Cerebral Cortex, January 2018;28: 184–198

doi: 10.1093/cercor/bhw366
Advance Access Publication Date: 26 November 2016
Original Article

ORIGINAL ARTICLE

Long-term In Vivo Calcium Imaging of Astrocytes Reveals Distinct Cellular Compartment Responses to Sensory Stimulation

Jillian L. Stobart[1,2,†], Kim David Ferrari[1,2,†], Matthew J. P. Barrett[1,2], Michael J. Stobart[1,2], Zoe J. Looser[1,2], Aiman S. Saab[1,2] and Bruno Weber[1,2]

[1]Institute of Pharmacology and Toxicology, University of Zurich, CH-8057 Zurich, Switzerland and [2]Neuroscience Center, University and ETH Zurich, CH-8057 Zurich, Switzerland

Address correspondence to Jillian L. Stobart, Institute of Pharmacology and Toxicology, University of Zurich, Winterthurerstrasse 190, 8057 Zurich, Switzerland. Email: jstobart@pharma.uzh.ch

[†]These authors contributed equally to this work.

Abstract

Localized, heterogeneous calcium transients occur throughout astrocytes, but the characteristics and long-term stability of these signals, particularly in response to sensory stimulation, remain unknown. Here, we used a genetically encoded calcium indicator and an activity-based image analysis scheme to monitor astrocyte calcium activity in vivo. We found that different subcellular compartments (processes, somata, and endfeet) displayed distinct signaling characteristics. Closer examination of individual signals showed that sensory stimulation elevated the number of specific types of calcium peaks within astrocyte processes and somata, in a cortical layer-dependent manner, and that the signals became more synchronous upon sensory stimulation. Although mice genetically lacking astrocytic IP3R-dependent calcium signaling (*Ip3r2*$^{-/-}$) had fewer signal peaks, the response to sensory stimulation was sustained, suggesting other calcium pathways are also involved. Long-term imaging of astrocyte populations revealed that all compartments reliably responded to stimulation over several months, but that the location of the response within processes may vary. These previously unknown characteristics of subcellular astrocyte calcium signals provide new insights into how astrocytes may encode local neuronal circuit activity.

Key words: calcium transients, GCaMP6s, somatosensory cortex, 2-photon microscopy, whisker barrels

Introduction

Astrocytes, the primary glial cell type in the cortex, may influence synaptic environments, neuronal metabolism, and local blood flow. However, debate exists over the astrocytic contribution to these mechanisms, particularly in vivo (Takata et al. 2011; Navarrete et al. 2012; Nizar et al. 2013; Bonder and McCarthy 2014; Otsu et al. 2015). Central to this debate is the physiological role of astrocyte intracellular calcium fluctuations that are considered a measure of astrocyte activity and are potentially linked to the modulation of neuronal function (Volterra et al. 2014).

Classical studies of astrocyte calcium signaling in vivo have used calcium indicator dyes, which primarily detect calcium surges within astrocyte somata (Wang et al. 2006; Takata and Hirase 2008; Nizar et al. 2013) but not fine processes (Shigetomi et al. 2013). Recently, in vivo calcium imaging has been greatly improved by the development of genetically encoded calcium indicators (GECIs), such as the GCaMP family, which can be

specifically expressed in astrocytes and label the entire cellular structure (Shigetomi et al. 2013; Gee et al. 2014; Kanemaru et al. 2014). This labeling of cortical, olfactory bulb, and hippocampal astrocytes has revealed spontaneous calcium signals that are diverse in their cellular localization (endfoot, soma, and process) and signal characteristics (Bonder and McCarthy 2014; Gee et al. 2014; Kanemaru et al. 2014; Asada et al. 2015; Otsu et al. 2015; Srinivasan et al. 2015; Tang et al. 2015). However, the relevance of this signal heterogeneity to astrocyte brain function remains unclear (Volterra et al. 2014).

Cortical astrocyte calcium signaling also occurs in response to sensory stimulation (Wang et al. 2006; Takata et al. 2011; Gee et al. 2014), and may encode neuronal responses to different patterns of sensory input (Volterra et al. 2014). Fine astrocyte processes are closely associated with synapses, and could respond to synaptic activity with discrete calcium signals that are confined to the local structure. Also, astrocyte calcium signals can be synchronized between different cellular compartments and neighboring cells (Takata and Hirase 2008). This synchronicity could be essential for astrocyte integration of activity from a cortical network. Additionally, astrocytes have been shown to have different levels of spontaneous activity between cortical layers (Takata and Hirase 2008), suggesting astrocyte populations may also have unique layer cyto-architectures similar to cortical neuronal networks (Petersen 2007).

Here, we investigated how astrocyte calcium signal heterogeneity may encode synaptic activity by examining astrocyte calcium signals evoked by sensory input in order to determine if subcellular regions (endfeet, somata, and processes) have similar responses, temporal synchronicity, and long-term stability. We imaged GCaMP6s in somatosensory astrocytes in vivo and developed novel analysis tools that enabled us to discriminate between spontaneous and sensory-evoked activity within the astrocyte population, characterize distinct peak types, and monitor astrocyte calcium signals over several months. Our results indicate that active regions within somatosensory astrocytes respond to sensory input with calcium signals of a particular shape, that these regions become more synchronized upon stimulation, and that the response varies between cortical layers. Furthermore, the overall response in all subcellular compartments was stable over several months. This work provides new insight into how calcium signaling in different astrocytic compartments may reflect local synaptic activation evoked by sensory stimulation.

Materials and Methods

Cloning and Virus Production

The GCaMP6s gene from pGP-CMV-GCaMP6s (a gift from Douglas Kim; Addgene plasmid #40 753; Chen et al. 2013) was cloned into a plasmid backbone containing AAV2 inverted terminal repeats, a short glial fibrillary acidic protein (GFAP) promoter (Gfa-ABC$_1$D or sGFAP; Lee et al. 2008), a β-globin intron, and poly adenylation signal (Mächler et al. 2016). This plasmid was packaged into adeno-associated virus (AAV) serotype 9 (AAV9-sGFAP-GCaMP6s) by the University of North Carolina Vector Core.

Animals

All experimental procedures were approved by the local veterinary authorities, conforming to the guidelines of the Swiss Animal Protection Law, Veterinary Office, Canton Zurich (Act of Animal Protection 16 December 2005 and Animal Protection Ordinance 23 April 2008). Mice were housed under an inverted 12-h light/dark cycle. Ip3r2 mice were maintained as a heterozygous line and genotypes were determined using previously reported mutant allele-specific primers (Li et al. 2005). Female C57BL/6 J (Charles River) or Ip3r2$^{-/-}$ mice with wild-type (WT) littermates (Ip3r2$^{+/+}$; Li et al. 2005; Di Castro et al. 2011) were surgically prepared at 8–10 weeks of age.

Head Post Implantation

Surgery was conducted as previously described (Mayrhofer et al. 2015). Under isoflurane (4% for induction, 1–2% for maintenance), animals were fixed in a stereotaxic frame and an incision was made along the midline to expose the skull. After cleaning the bone, a bonding agent (Prime & Bond) and several layers of light-cured dental cement (Tetric EvoFlow) were applied to the skull and polymerized with blue light. An aluminum head post was attached to the cement at the back of the head. The skull over the left somatosensory cortex was left exposed for later craniotomy and virus injection.

Intrinsic Optical Imaging

Intrinsic optical imaging (IOI) was used to map the somatosensory areas for proper localization of the virus injection and subsequent 2-photon imaging. Two days following the head post-surgery, the skull over the left cortex was moistened with a water-based gel to increase bone transparency, and covered with a glass coverslip. Under 630 nm illumination, images were acquired using a 12-bit CCD camera (Pixelfly VGA, PCO Imaging) focused 0.4 mm below the cortical surface. Whisker (10 Hz) or hindpaw stimulation (400 μA, 1 ms, 4 Hz, 5 s) elicited increased blood flow to the corresponding sensory area, which was observed as increased light absorption. IOI measurements were repeated 2 weeks after surgery through the cranial window to create a somatotopic map that was used for appropriate localization during 2-photon imaging.

Virus Injection and Chronic Window Implantation

Under midazolam (5 mg/kg), fentanyl (0.05 mg/kg), and medetomidine (0.5 mg/kg) anesthesia, a craniotomy was cut over the primary sensory cortex using the IOI map as a reference. A pipette and hydraulic pump were used to inject AAV9-GFAP-GCaMP6s virus (300 nL of 3.2×10^{12} particles/mL at 50 nL/min) into the hindpaw and/or whisker barrel areas at a depth of 350–400 μm. A square coverslip (3 × 3 mm) was lightly pressed on the exposed brain and fixed with dental cement to the head cap.

Two-Photon Imaging

Imaging commenced 3 weeks after virus injection using a custom-built 2-photon laser-scanning microscope. A ×20 water immersion microscope objective was used (W Plan-Apochromat 20×/1.0 DIC VIS-IR, Zeiss). GCaMP6s was excited at 940 nm with a Ti:sapphire laser (Chameleon Ultra II; Coherent or InSight DeepSee; Spectra-Physics) with power between 10 and 30 mW. Fluorescence emission was detected with a GaAsP photomultiplier module (Hamamatsu Photonics) with a band-pass filter BrightLine HC 520/50 and a short pass filter BrightLine 750/sp (Semrock). The 2-photon laser-scanning microscope was controlled by a customized version of "ScanImage" (r3.8.1; Janelia Research Campus).

All imaging was conducted under isoflurane anesthesia (1–1.5%). Detailed anatomical images (512 × 512 pixels) of each field of view were collected at 0.74 frames per second. Images

(256 × 256 or 128 × 128 pixels) were acquired at a frequency of 1.48–2.96 frames per second. Multiple fields of view in both cortical layer 1 (depth ~30–100 μm) and cortical layer 2/3 (depth ~150–250 μm) were recorded in each animal. Single whiskers were threaded into a glass capillary attached to a custom-built piezoelectric stimulator (T223-H4CL-303X; Piezo Systems) and deflected at different frequencies of stimulation (10, 20, 40, and 90 Hz; 1 or 8 s duration) during imaging. The contralateral hindpaw was electrically stimulated by a 4 Hz (1 ms pulse), 400 μA current for 5 s. Given that all mice had a chronic cranial window implanted, we were able to conduct multiple imaging sessions for each animal.

Image Analysis and Statistics

Image analysis was performed using ImageJ (Schneider et al. 2012) and MATLAB R2014b (MathWorks). For each field of view, all images were aligned using a 2D convolution engine to account for $x-y$ drift in time. Background noise was defined as the bottom fifth percentile pixel value in each frame and was subtracted from every pixel. Regions of interest (ROIs) were selected by 2 methods: our customized implementation of an activity-based algorithm (Ellefsen et al. 2014) and manual selection in ImageJ of somata and endfeet ROIs using high resolution (512 × 512 pixel) anatomical images. In the activity-based algorithm, a 2D spatial Gaussian filter with $\sigma xy = 3$ pixels (2.86 μm) and a temporal moving average filter with a width of 3 frames were applied to all images to reduce noise. A moving threshold for each pixel was defined in the filtered stack as the mean intensity plus 7 times the standard deviation of the same pixel during the preceding 30 frames. Using this sliding box-car approach, active pixels were identified as those that exceeded the threshold. Active pixels were grouped within a radius of 5 pixels (4.75 μm) in space and 2 frames in time. The 3D mask of active pixels was summed along the temporal dimension, normalized, and thresholded at $\theta = 0.3$ to make a 2D activity ROI mask. Raw image data from pixels within each 2D ROI were statistically compared with pixels surrounding the ROI ($P < 0.05$ by one-way ANOVA) to exclude false positives. Activity ROI masks and manually selected ROI masks (somata and endfeet) were compared and overlapping regions were excluded from the activity mask to ensure each ROI was unique. When comparing different stimulation conditions in each field of view, ROI masks were combined to measure the same ROIs in all conditions. A signal vector (dF/F) was calculated relative to the baseline fluorescence in the first 5 s of the trial. This vector was low-pass filtered using a moving average filter with a cut-off frequency of ~0.03 Hz to locate plateau peaks and measure their features, such as maximum amplitude and duration (findpeaks function; MATLAB). Singlepeak and multipeak signals were identified by applying a digital band-pass filter with passband frequencies $f1 = 0.0286$ Hz and $f2 = 0.1$ Hz to the dF/F signal vector before running MATLAB findpeaks function. We also used a seed-based correlation analysis to correlate the signal vector (dF/F) for each ROI with the vectors from all other ROIs in the same field of view and examined the mean Pearson's correlation coefficient across trials. For chronic recordings, animals were imaged over 2 months at 4 different time points. The distance between ROI centroids from different imaging days was calculated and ROIs were considered to be the same where this distance was less than the radius of the mean ROI area.

All statistics were performed in R (version 3.1.2) using the lme4 package (Bates et al. 2015) for linear mixed-effects models. As fixed effects, we used stimulus condition (with/without stimulation), ROI type (endfoot, soma, or process), and cortical layer and also tested the interaction of these effects. As random effects, we had intercepts for individual animals, fields of view, and ROIs. Likelihood ratio tests comparing models with fixed effects against models without fixed effects were used to determine the model with the best fit while accounting for the different degrees of freedom. Visual inspection of residual plots did not reveal any obvious deviations from homoscedasticity or normality. All data were reported and plotted as uncorrected means and standard error of the means (SEM). P values for different parameter comparisons were obtained using the lsmeans or multcomp (Hothorn et al. 2008) packages with Tukey post hoc tests.

Immunohistochemistry

Mice were anesthetized with pentobarbital (>50 mg/kg) and transcardially perfused with 2% paraformaldehyde (PFA). Brains were post-fixed in 4% PFA for 3 h and cryoprotected with 30% sucrose in phosphate buffered saline for 24 h. Free-floating sections (40 μm) were cut with a freezing microtome. Slices were incubated with rabbit anti-GFAP antibody (Z0334; DakoCytomation, DK), rabbit anti-ionized calcium binding adapter molecule 1 (Iba1) (WAKO) or anti-rat CD68 (MCA1957GA, Serotec) together with chicken anti-GFP antibody (GFP-1020, Aves Labs). Secondary antibodies for red and green (goat anti-rabbit Alexa Fluor 660 and goat anti-chicken Alexa Fluor 488; Life Technologies) were then added. Images of the sections were collected with a Zeiss LSM710 confocal microscope.

Results

Astrocyte Subcellular Regions are Spontaneously Active and Exhibit Distinct Signaling Characteristics

To visualize astrocyte cytosolic calcium signals in the mouse somatosensory cortex, we injected AAV9-sGFAP-GCaMP6s virus, implanted a chronic cranial window, and imaged the animals by 2-photon microscopy 3 weeks later while under isoflurane anesthesia (Fig. 1A). To analyze the GCaMP6s calcium signals recorded during 2-photon imaging, we developed a semi-automated image analysis where active ROIs were identified in time and space (Ellefsen et al. 2014) and condensed into a 2D mask (Fig. 1B). Somata and endfeet regions were selected by hand from visible structures in baseline images. The majority of ROIs identified by the automated analysis were located in the fine cellular processes, but those that overlapped with manually selected somata and endfeet ROIs were excluded to ensure each ROI was distinct. Process ROIs had a greater number of spontaneous signals per minute (0.65 ± 0.02 signals/min; $P < 0.0001$; Fig. 1D) and a larger mean amplitude (0.35 ± 0.01-fold; $P < 0.0001$; Fig. 1E) than endfeet or somata ROIs. However, the mean duration of spontaneous signals from somata ROIs (9.58 ± 0.32 s) was greater than processes ($P = 0.0175$) and endfeet ($P = 0.0255$; Fig. 1F). A previous study comparing Oregon Green BAPTA-AM labeled rat astrocytes in different cortical layers showed layer 1 somata were more spontaneously active with larger signal amplitudes than layer 2/3 cells (Takata and Hirase 2008). Overall, we did not observe significant differences in spontaneous signal amplitude, duration, or number of signals per minute between layers; however, layer 1 somata tended to have more signals per minute than layer 2/3 somata (Supplementary Fig. S1A–C). Notably, there was also no difference in the number of ROIs per area (mm^2) between different layers (Supplementary Fig. S1D).

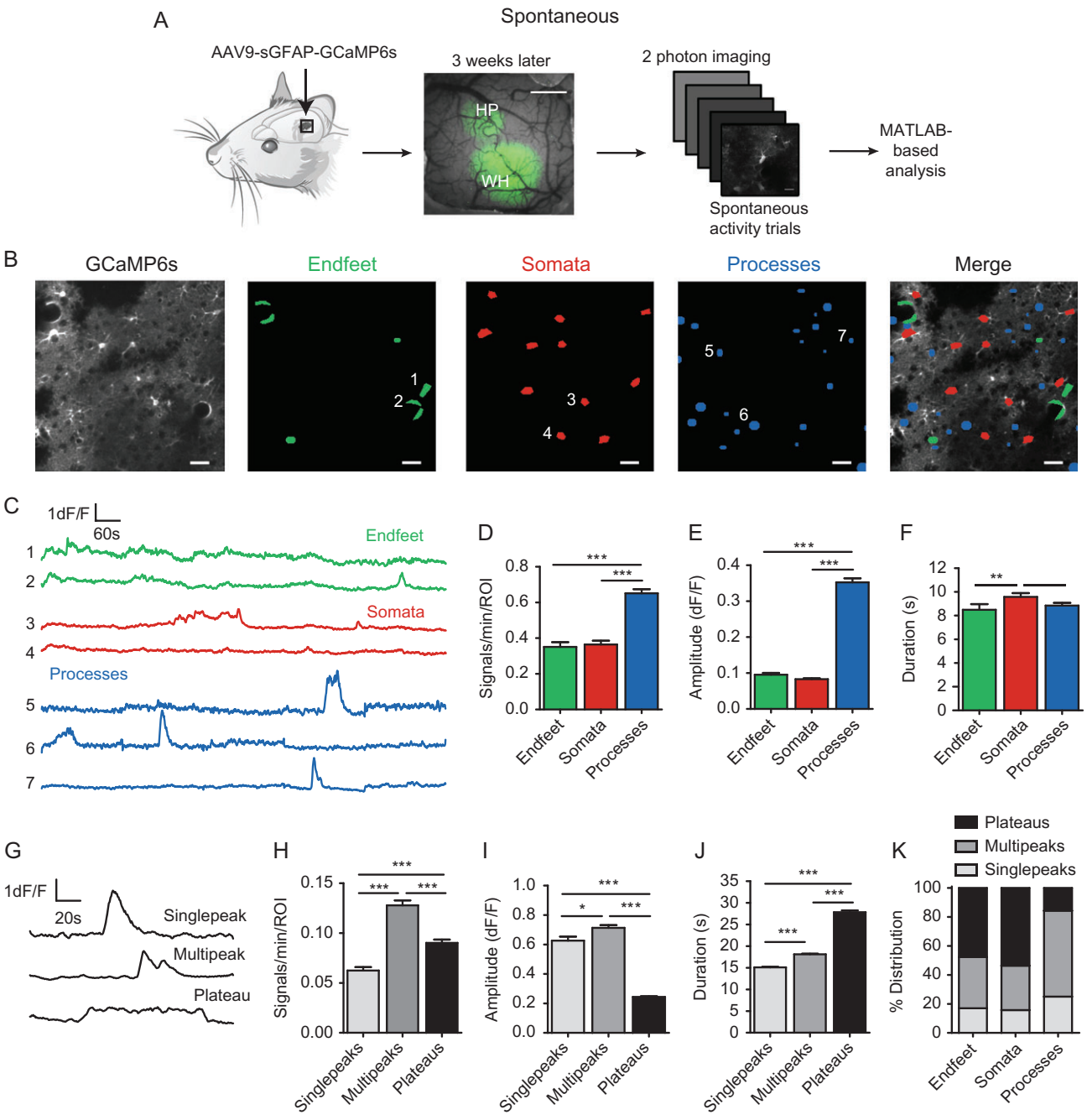

Figure 1. Astrocyte subcellular calcium domains exhibit distinct spontaneous signaling characteristics. (*A*) Left: AAV9-sGFAP-GCaMP6s virus was injected into the mouse somatosensory cortex. Middle: example image of the chronic cranial window showing GCaMP6s expression in the whisker (WH) and hindpaw (HP) areas 3 weeks post-injection. Scale bar is 500 μm. Right: images from anesthetized animals without stimulation were collected by 2-photon microscopy and analyzed in MATLAB. (*B*) End foot (green) and soma (red) ROIs were selected manually based on visible structures. Active calcium ROIs were identified algorithmically and primarily localized in astrocyte processes (blue). Scale bar is 30 μm. (*C*) Example traces of spontaneous activity from each ROI type. (*D–F*) Mean number of signals per minute, amplitude, and duration of signals per ROI (endfeet: $n = 167$ ROIs; somata: $n = 393$ ROIs; processes: $n = 501$ ROIs; 12 mice). (*G*) Example traces of the 3 peak types: singlepeaks, multipeaks and plateaus. (*H*) Mean number of each peak type per minute per ROI ($n = 1061$ ROIs; 12 mice). (*I,J*) Mean amplitude and duration of the different peak types (singlepeaks: $n = 1018$ signals; multipeaks: $n = 2283$ signals; plateaus: $n = 1538$ signals; 12 mice). (*K*) Relative percentages of each peak type within the different ROI types. Example traces were smoothed with a 5-point moving average. Bar graphs are uncorrected mean ± SEM. $^{*}P < 0.05$, $^{***}P < 0.001$. Statistics calculated using linear mixed models. See also Supplementary Fig. S1.

Based on their shape, GCaMP6s signal peaks were also divided into 3 different classes: singlepeaks, multipeaks, and plateaus (Fig. 1*G*; Bonder and McCarthy 2014). These peak types were classified based on band-pass (singlepeaks and multipeaks) and low-pass filtering (plateaus) of the signal fluorescence vector. Singlepeaks were identified as short, individual peaks, while multipeaks were oscillating signals with multiple maxima close together in time. Plateau signals were identified as long, slower signals that had a small slope (<0.0015 DF/s) at the peak maximum (Fig. 1*G*). Of all spontaneous peaks, 21% were

singlepeaks, 47.2% were multipeaks, and 31.8% were plateaus (n = 4839 signals; 12 mice). Multipeaks were the most frequent peak type when considering the overall number of peaks per minute per ROI ($P < 0.0001$; Fig. 1*H*). Multipeaks also had the largest mean amplitude (0.71 ± 0.02-fold; $P = 0.0335$ vs. singlepeaks), while plateaus had a smaller mean amplitude (0.24 ± 0.01-fold) compared with both multipeaks ($P < 0.0001$) and singlepeaks (0.62 ± 0.03-fold; $P < 0.0001$; Fig. 1*I*). Plateau peaks had the longest mean duration (27.83 ± 0.42 s; $P < 0.0001$), while multipeaks (18.12 ± 0.11 s) were longer than singlepeaks (15.1 ± 0.12 s; $P < 0.0001$; Fig. 1*J*). The distribution of peak types within individual ROI groups was also different with endfeet and somata favouring plateaus (endfeet: 47.7% of 587 signals; somata: 53.6% of 1556 signals; 12 mice) and processes favouring multipeaks (59.3% of 2696 signals; 12 mice; Fig. 1*K*). Process ROI peaks had different shapes compared with endfeet and somata peaks, with larger mean amplitudes (Supplementary Fig. S1*E*) and significantly greater duration for multipeaks and plateaus (Supplementary Fig. S1*F*).

These calcium signals were recorded from healthy astrocytes, since GCaMP6s expression co-localized with astrocyte dye, SR101, 90 min after intravenous dye injection (Fig. 2*A*; Appaix et al. 2012). Also, cortical virus injections did not induce reactive astrogliosis or microglial activation, as GFAP and Iba1 labeling was similar within the injection site and in the contralateral (non-injected) hemisphere (Fig. 2*B–E*). Additionally, we did not detect an increase in CD68 staining, further supporting a lack of microglial activation (Supplementary Fig. S2).

Astrocytes Respond to Sensory Stimulation

In order to study the local astrocyte response to somatosensory activation, we used 2 different stimulation paradigms: electrical hindpaw stimulation (400 µA at 4 Hz for 5 s, Movie 1) and single whisker deflection (1 s duration) at different frequencies known to mimic "stick-slip" events from whisking on textured surfaces (Movie 2; Wolfe et al. 2008; Jadhav et al. 2009; Mayrhofer et al. 2015). We directly compared trials with sensory stimulation to trials without stimulation to identify stimulus-evoked responses. This was done by running the semi-automated ROI selection on each group of trials independently and then combining the ROIs to make an overall ROI mask that included endfeet, somata, and process ROIs. In Figure 3*B*, process ROI masks were generated for the same field of view from trials with 1 of 5 frequencies of whisker stimulation: 0 Hz (no stimulation), 10, 20, 40, and 90 Hz. The final combined mask (sum of all process masks, plus the manually selected endfeet and somata mask) was then applied to all images to collect signal information from the same ROI population for each stimulus condition. When considering the entire ROI population (endfeet, somata, and processes together), 90 Hz whisker stimulation ($P = 0.0025$) and hindpaw stimulation ($P < 0.0001$) increased the mean number of signals per minute per ROI compared with trials without stimulation (Fig. 3*C*). Lower frequencies of whisker stimulation (10–40 Hz) did not increase the number of peaks per ROI. We attributed the absence of whisker stimulation-evoked responses at these frequencies to the high degree of spontaneous activity within many ROIs. Therefore, we defined a ROI as "responding" if it contained peaks in the 30 s following the onset of sensory stimulation in any trial ("activity window"); ROIs that did not meet this criterion were defined as "spontaneous". In the hindpaw area, ~80% of the 297 ROIs (5 mice, including endfeet, somata, and processes) showed a response in the activity

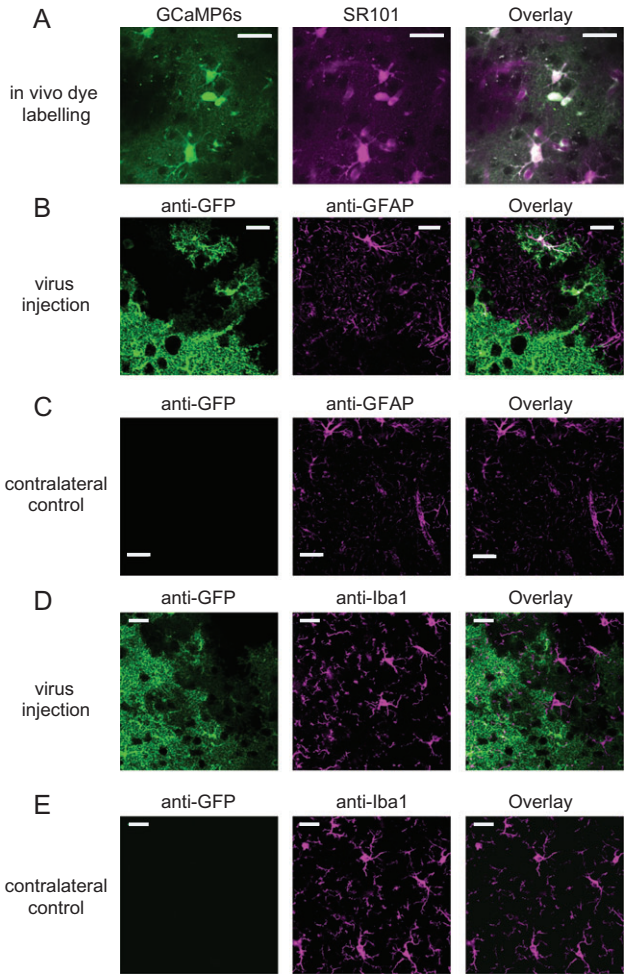

Figure 2. Astrocytic GCaMP6s expression in vivo. (*A*) Images of GCaMP6s expression and sulforhodamine 101 (SR101), a dye known to label astrocytes, taken 90 min after intravenous SR101 injection. Scale bar is 30 µm. (*B*) Immunohistochemistry of brain slices from AAV9-GFAP-GCaMP6s injected mice. The virus injection site (GCaMP6s) was further stained with an anti-GFP antibody, and astrocytes were labeled with anti-GFAP. Scale bars are 20 µm. (*C*) Virus injected hemispheres were compared with GFAP staining on the contralateral (non-injected control) side. (*D*) Immunohistochemistry for microglial infiltration. The virus injection site was further stained with an anti-GFP antibody and microglia were labeled with anti-Iba1. (*E*) Virus injected hemispheres were compared with the contralateral side. Scale bars are 20 µm. See also Supplementary Fig. S2.

window following electrical stimulation, while ~44% of 492 barrel cortex ROIs (5 mice) responded to single whisker deflection of any frequency (10–90 Hz). The time to peak maximum after the onset of stimulation was similar at 12.95 ± 0.28 s for hindpaw stimulation (n = 804 peaks from 5 mice) and 13.89 ± 0.32 s for whisker deflection (n = 769 peaks from 5 mice; $P = 0.668$). When averaging the data from all trials, responding ROIs had more signals per minute (Fig. 3*D*) and greater mean signal amplitudes (Fig. 3*E*) and duration (Fig. 3*F*) during both types of stimulation (hindpaw and various whisker deflection frequencies) compared with no stimulation trials. In a recent study, we characterized the neuronal population response to different frequencies (0, 10, 40, 90, and 110 Hz) of whisker stimulation through neuronal calcium imaging (Mayrhofer et al. 2015). We observed that the calcium signal amplitude and response probability increased sublinearly with increasing stimulation frequency; however, different stimulation frequencies elicited

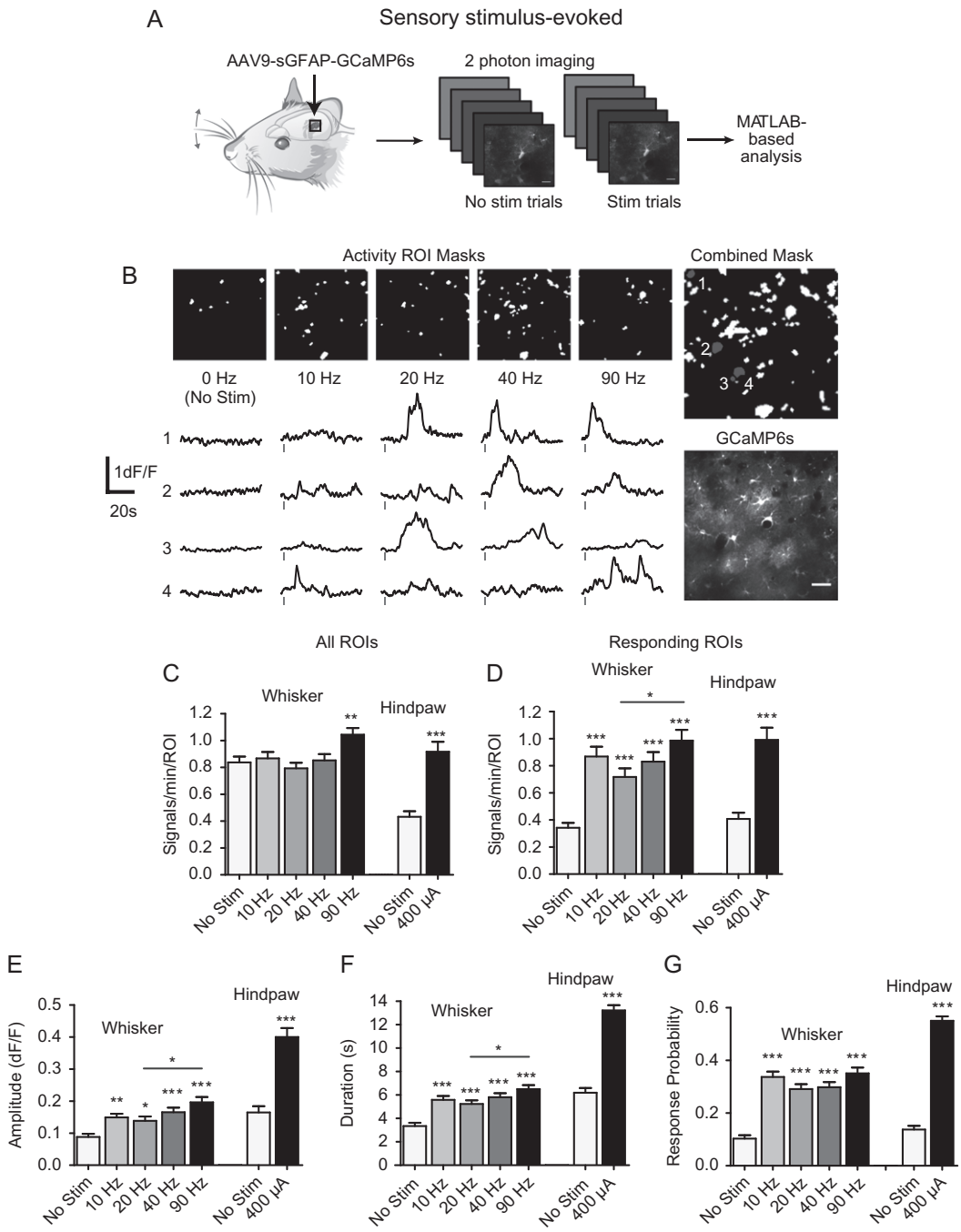

Figure 3. Astrocytes respond to sensory stimulation. (*A*) GCaMP6s positive astrocytes in the hindpaw and whisker cortical areas were imaged by 2-photon microscopy. Images from trials with and without sensory stimulation were compared. (*B*) Activity ROI masks from trials without stimulation (0 Hz) and with brief (1 s) single whisker deflection (10, 20, 40, 90 Hz; top) were pooled together (combined mask; right). Scale bar is 30 µm. Lower: example traces (smoothed with a 5-point moving average) from 4 ROIs (gray) for each frequency of stimulation. Lines below indicate stimulus. (*C*) Mean number of signals per minute per ROI from the total population (endfeet, somata, and processes) following hindpaw (400 µA; 1 ms; 4 Hz; for 5 s) or whisker stimulation (10, 20, 40, 90 Hz; 1 s). (*D*) Mean number of signals per minute per ROI from responding ROIs with and without hindpaw ($P < 0.0001$; 237 ROIs; 5 mice) or whisker stimulation (all comparisons to no stim: $P < 0.0001$; 218 ROIs; 5 mice). (*E*) Mean amplitude for responding ROIs comparing hindpaw ($P < 0.0001$; 237 ROIs; 5 mice) or whisker stimulation (10 Hz: $P = 0.0065$; 20 Hz: $P = 0.0418$; 40 Hz: $P < 0.0001$; 90 Hz: $P < 0.0001$; 218 ROIs; 5 mice) to no stimulation trials. (*F*) Mean signal duration for responding ROIs with and without hindpaw ($P < 0.0001$) or whisker stimulation (all comparisons to no stim: $P < 0.0001$). (*G*) Mean response probability (i.e., the fraction of trials with a peak in the activity window) following hindpaw or whisker stimulation from responding ROIs ($P < 0.0001$ for all comparisons to no stim). Bar graphs are uncorrected mean ± SEM. *$P < 0.05$, **$P < 0.01$, ***$P < 0.001$. Statistics calculated using linear mixed models. See also Supplementary Movies 1 and 2 and Supplementary Fig. S3.

similar cortical network activation in the same neuronal populations (Mayrhofer et al. 2015). In the present study, astrocytes did not demonstrate a sublinear, graded response to increasing whisker stimulus frequency, but 90 Hz stimulation elicited the largest mean amplitude, duration, and number of signals per minute (Fig. 3*D–F*) in responding ROIs. We also calculated the response probability for each astrocyte ROI (i.e., the fraction of trials with a signal in the activity window) and found that the

mean probability was less than 1.0. This suggests astrocytes did not respond to the stimulus in every trial, but they responded on average in ~30% of whisker trials and ~55% of hindpaw trials (Fig. 3G). Sensory stimulation did not elicit a global astrocytic response, as no change in number of signals per minute, amplitude, or duration was detected in responding whisker barrel ROIs during hindpaw stimulation and responding hindpaw ROIs during whisker stimulation (Supplementary Fig. S3). Since whisker deflection is non-noxious and more physiological than hindpaw stimulation and 90 Hz stimulation evokes a strong neuronal response (Mayrhofer et al. 2015), we used 90 Hz whisker stimulation for 8 s to evoke the maximal response in the remaining experiments.

Astrocyte Subcellular Compartments Respond Differentially to Stimulation

We also investigated the stimulus-evoked response in different astrocyte subcellular compartments. In the entire ROI population, whisker (90 Hz for 8 s) stimulation-evoked responses in endfeet and somata were masked by spontaneous activity and only processes showed a significant increase in the number of signals per minute compared with no stimulation trials ($P = 0.003$; Fig. 4A). To better study stimulus-evoked responses, responding ROIs with a peak in the activity window were identified in the endfoot, soma, and process subpopulations. We first compared the mean ROI area (μm^2) for responding and spontaneous ROIs (Fig. 4B). Endfeet and somata were selected based on cellular structure, and we did not observe differences in the area of spontaneous or responding ROIs ($P = 0.999$). However, process ROIs were selected based on activity and responding processes had a larger mean area than spontaneous processes ($P < 0.0001$; Fig. 4B), similar to light-evoked astrocyte calcium signals in the visual cortex (Asada et al. 2015). Processes also reportedly have an earlier calcium signal onset time after stimulation (Wang et al. 2006; Gee et al. 2014). When considering only the responding ROIs in each subcellular compartment, we found processes had the fastest mean time to reach peak maximum after 90 Hz whisker stimulation (14.41 ± 0.35 s), but there was no significant difference ($P = 0.999$ for all comparisons) between process, endfoot (14.73 ± 0.75 s), and soma (15.07 ± 0.51 s) peak times. Responding processes showed an increase in mean signal amplitude upon whisker stimulation ($P < 0.0001$), while we did not observe a change in amplitude in responding endfeet ($P = 0.2285$) or somata ($P = 0.3613$; Fig. 4D). The number of signals per minute (Fig. 4C) and mean signal duration (Fig. 4E) increased in all responding ROI types upon 90 Hz whisker stimulation ($P < 0.0001$). We also observed a similar mean response probability for responding endfeet, somata, and process ROIs (Fig. 4F).

Sensory Stimulation Induces Layer-Dependent Changes in the Relative Number, Not the Nature, of Different Peak Types

To investigate the underlying changes driving the overall increase in signal frequency, amplitude, and duration in the different responding subcellular compartments, we further separated the responses by peak type and cortical layer. Upon sensory stimulation, the shape of the peak types (singlepeaks, multipeaks, and plateaus) did not change in amplitude or duration in any of the subcellular compartments (Supplementary Fig. S4). When considering the number of different peak types, the number of singlepeaks per minute remained unchanged in all responding ROI types (endfeet, somata, or processes) and layers (Fig. 5A–C). However, somata in layer 2/3 ($P = 0.0014$; $n = 94$ ROIs; 10 mice) and processes in both cortical layers ($P < 0.0001$, layer 1, $n = 248$ ROIs; $P < 0.0001$, layer 2/3, $n = 174$ ROIs; 10 mice) had a higher number of multipeaks per minute during stimulation trials (Fig. 5E,F). Plateau signals were also prominent in responding layer 2/3 somata during whisker deflection trials ($P < 0.0001$; $n = 94$ ROIs; 10 mice; Fig. 5H). There was some evidence of an increased number of multipeaks in layer 1 endfeet ($P = 0.0654$; $n = 41$ ROIs; 10 mice; Fig. 5D) and an increased number of plateaus in layer 1 somata ($P = 0.1752$; $n = 114$ ROIs; 10 mice; Fig. 5 H), but they were not significantly different from trials without stimulation.

Astrocytes from *Ip3r2*$^{-/-}$ Mice also Respond to Sensory Stimulation

Previous studies have shown that inositol-1,4,5-trisphosphate (IP_3)-dependent calcium release from the endoplasmic reticulum (ER) is important for astrocyte calcium signaling (Petravicz et al. 2008; Nizar et al. 2013; Takata et al. 2013; Srinivasan et al. 2015). We examined the involvement of this pathway in sensory stimulation-evoked astrocyte responses by expressing GCaMP6s in astrocytes from *Ip3r2*$^{-/-}$ mice and WT littermate controls (Li et al. 2005) and selecting subcellular ROIs in the same manner as previous experiments (manual selection for endfeet and somata ROIs and automated detection for processes). *Ip3r2*$^{-/-}$ astrocytes were less spontaneously active, as we detected fewer process ROIs in each field of view and these ROIs tended to have a smaller area (Supplementary Fig. S5A,B). We also detected fewer spontaneous singlepeaks and multipeaks in *Ip3r2*$^{-/-}$ mice (Supplementary Fig. S5C). The shape of different spontaneous calcium signal peaks was not significantly different between WT and knockouts, other than a slightly decreased duration of plateau signals in *Ip3r2*$^{-/-}$cells (Supplementary Fig. S5D,E). Upon 90 Hz whisker stimulation, we were able to identify responding endfeet, somata, and process ROIs in *Ip3r2*$^{-/-}$ and WT astrocytes based on our previous criteria (peak in the activity window following stimulation; Fig. 3). *Ip3r2*$^{-/-}$ responding ROIs had an increased number of signals per minute and longer mean signal duration compared with trials without stimulation ($P < 0.0001$; Fig. 6 A, C). The mean signal amplitude in responding *Ip3r2*$^{-/-}$ ROIs also tended to increase, but was not significantly different between trials with and without stimulation ($P = 0.1673$; Fig. 6B). When comparing stimulus-evoked responses from WT and *Ip3r2*$^{-/-}$ ROIs, the mean amplitude and duration were not significantly different ($P = 0.1365$ and $P = 0.5836$, respectively; Fig. 6B, C), and WT and *Ip3r2*$^{-/-}$ ROIs responded to stimulation with a similar probability ($P = 0.4456$; Fig. 6D). However, *Ip3r2*$^{-/-}$ ROIs had fewer signals per min than WT ROIs ($P = 0.0043$; Fig. 6A). When considering individual peaks, the mean time to reach peak maximum after 90 Hz whisker stimulation was similar for WT (15.77 ± 0.35 s) and *Ip3r2*$^{-/-}$ (15.79 ± 0.42 s) signals ($P = 0.1124$). Overall, peaks from each genotype that occurred during stimulation trials had a similar peak shape (no appreciable change in amplitude or duration; data not shown). Furthermore, WT and *Ip3r2*$^{-/-}$ displayed a similar number of stimulus-evoked singlepeaks and plateaus in each cellular compartment and cortical layer (data not shown); however, whisker deflection evoked fewer multipeaks in *Ip3r2*$^{-/-}$ astrocyte subcellular compartments particularly in layer 2/3 (endfeet: WT vs. *Ip3r2*$^{-/-}$, $P = 0.0017$; somata: WT vs. *Ip3r2*$^{-/-}$, $P = 0.0004$; processes: WT vs. *Ip3r2*$^{-/-}$, $P < 0.0001$; Fig. 6E–G).

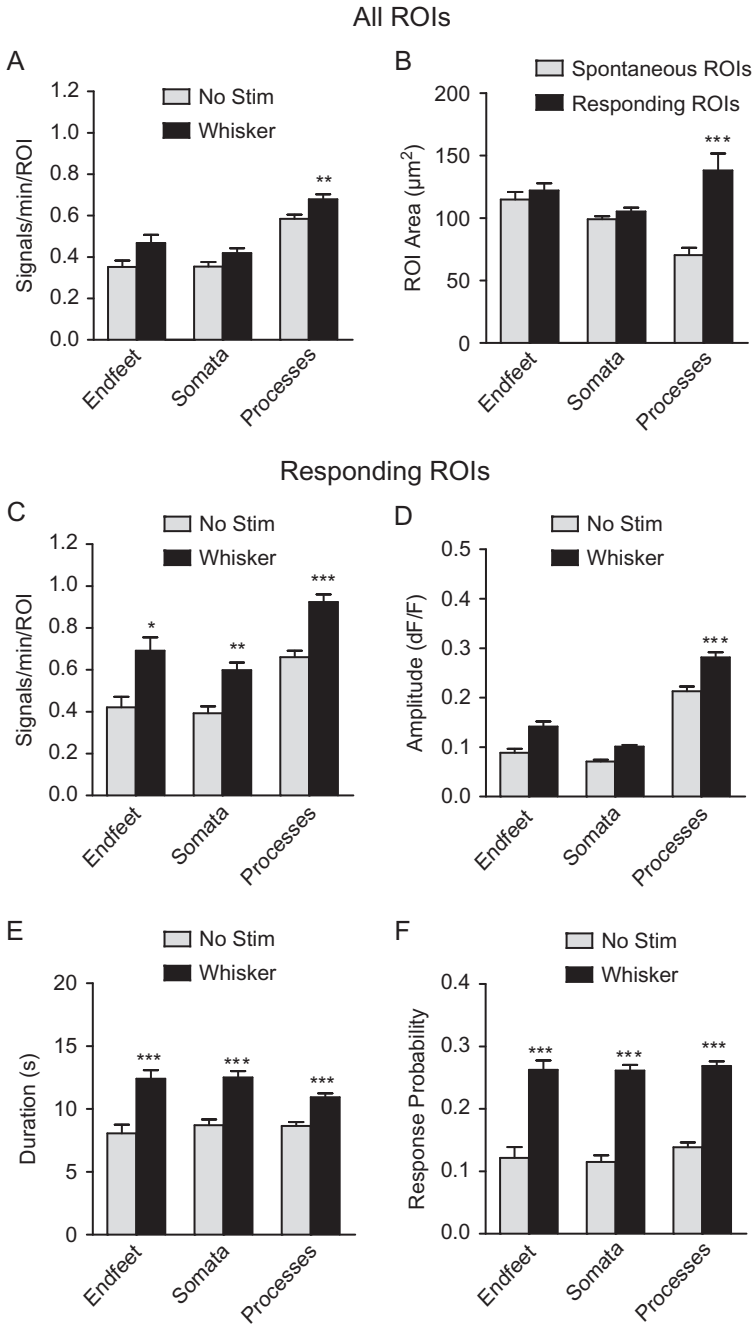

Figure 4. Astrocyte processes respond differently than endfeet and somata to sensory stimulation. (*A*) Mean number of signals per minute per ROI for all endfoot (n = 166 ROIs), soma (n = 403 ROIs), and process (n = 820 ROIs) ROIs following 90 Hz whisker deflection for 8 s (12 mice). (*B*) Mean ROI area (μm^2) for spontaneous and responding ROIs from endfeet, somata, and processes. (*C*) Mean number of signals per minute for responding endfeet (P = 0.0224; n = 85 ROIs), somata (P = 0.0029; n = 208 ROIs), and processes ($P < 0.0001$; n = 420 ROIs) with or without whisker stimulation (90 Hz; 8 s). (*D–F*) Mean amplitude, duration, and response probability for responding ROIs (endfeet, somata, and processes) with or without whisker stimulation. Bar graphs are uncorrected mean ± SEM. $^*P < 0.05$, $^{**}P < 0.01$, $^{***}P < 0.001$. Statistics calculated using linear mixed models.

Astrocyte Regions Become More Correlated in Response to Sensory Stimulation

To characterize the temporal dynamics of the GCaMP6s calcium signals, we conducted a pairwise correlation analysis on the fluorescence signal (dF/F), where traces for each ROI were compared with traces from all other ROIs in the same field of view (Fig. 7A). Overall, ROIs were weakly correlated in trials without stimulation (Pearson coefficient, $\rho = 0.17 \pm 0.0008$; n = 27 956 pairs from 10 mice). The mean correlation increased upon whisker stimulation ($\rho = 0.20 \pm 0.0008$; $P < 0.0001$; Fig. 7C), as shown by a shift in the cumulative fraction (Fig. 7B), suggesting an increase in network synchronicity. When we considered responding ROIs and spontaneous ROIs, we created 3 pair groups—spontaneous vs. spontaneous ROIs, spontaneous vs. responding ROIs, and responding vs. responding ROIs. All pair groups showed an increase in correlation in trials with whisker stimulation

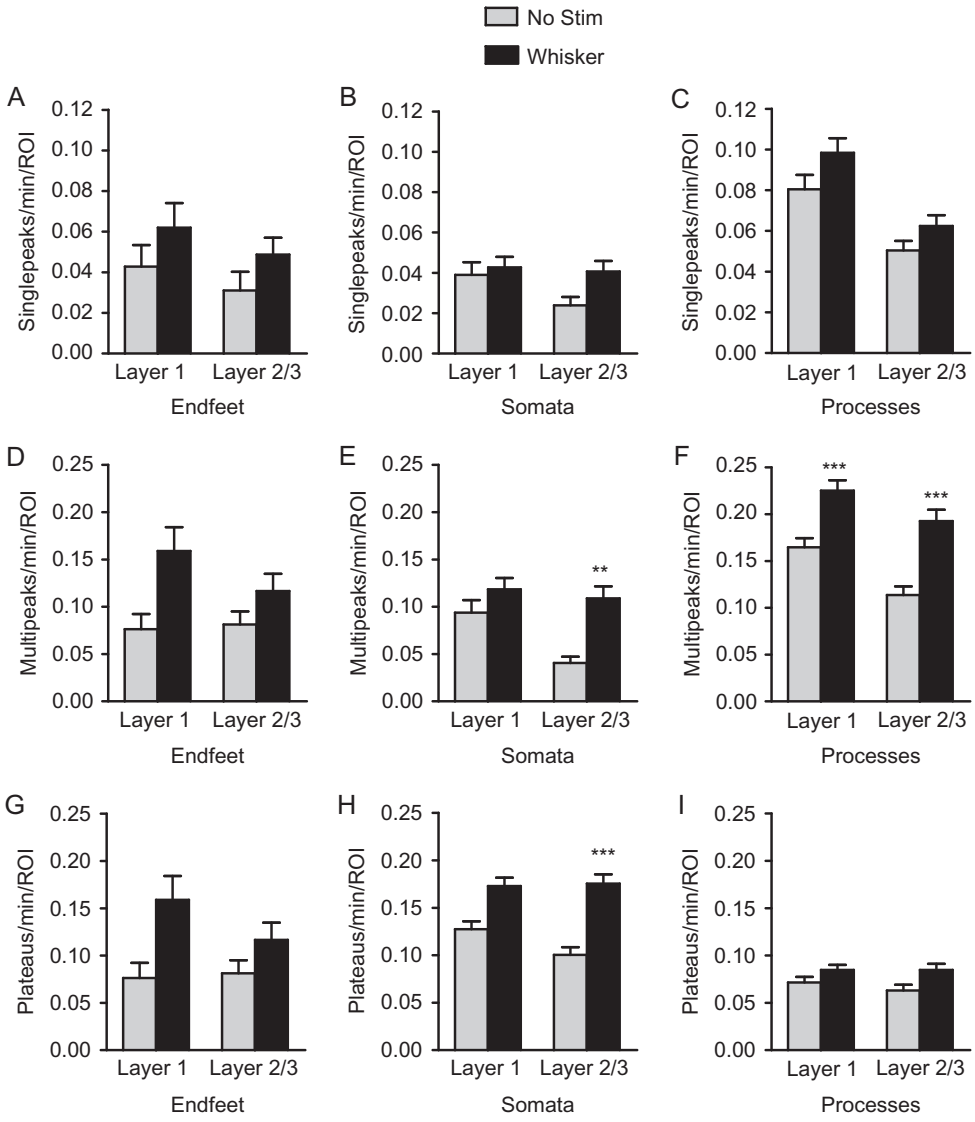

Figure 5. Responding ROIs have more signal peaks during sensory stimulation trials. (*A–I*) Mean number of peaks per minute, averaged across trials from each responding ROI type in layer 1, or layer 2/3 with (dark gray bars) or without (light gray bars) 90 Hz whisker stimulation (8 s). Singlepeaks: top row, multipeaks: middle row, plateaus: bottom row. Endfeet: left column; somata: middle column; processes: right column. Bar graphs are uncorrected mean ± SEM. **$P < 0.01$, ***$P < 0.001$. Statistics calculated using linear mixed models. See also Supplementary Fig. S4.

compared with trials without stimulation ($P < 0.0001$); however, responding ROI pairs were significantly more correlated in stimulation trials than spontaneous pairs or spontaneous vs. responding pairs ($P < 0.0001$, Supplementary Fig. S6*A*).

We also considered the pairwise signal correlations of responding ROIs separated by ROI type. Endfeet and somata pairs (endfeet vs. endfeet, somata vs. somata, and endfeet vs. somata) were more correlated overall than process pairs (processes vs. processes, processes vs. somata, and processes vs. endfeet; $P < 0.0001$; Supplementary Fig. 6*B*) in both no stimulation and stimulation trials. Upon whisker stimulation, all responding ROI pairs showed an increase in correlation compared with no stimulation trials (Supplementary Fig. 6*B*).

Long-term Stability of Endfeet and Somata Responses

Previously, our group has shown that a neuronal subpopulation consistently responds to whisker stimulation over several months (Mayrhofer et al. 2015), and we examined if astrocytes have a similar stability by imaging the same astrocyte population at different time points. Images from each session were spatially aligned to the images from the first time point (Day 0) to ensure that the field of view was the same for ROI selection across all time points (Fig. 8*A*). The corrected images were used to generate automated activity ROI masks for each time point, and the distances between ROI centroids from each imaging day were compared to find ROIs with multiple occurrences (overlapping ROIs, Fig. 8*B*). We grouped ROIs of particular types (endfeet, somata, and processes) with multiple occurrences based on the number of days within the 4 different time points that they showed a response to stimulation (Fig. 8*C*). Spontaneous ROIs did not respond to stimulation on any day (0 days group). ROIs that responded to stimulation only on 1 day (Day 0, 4, 18, or 67) were included in the 1 day group. ROIs that demonstrated a response at 2 or 3 different time points (2 and 3 days group) could occur on consecutive days (e.g., Day 0

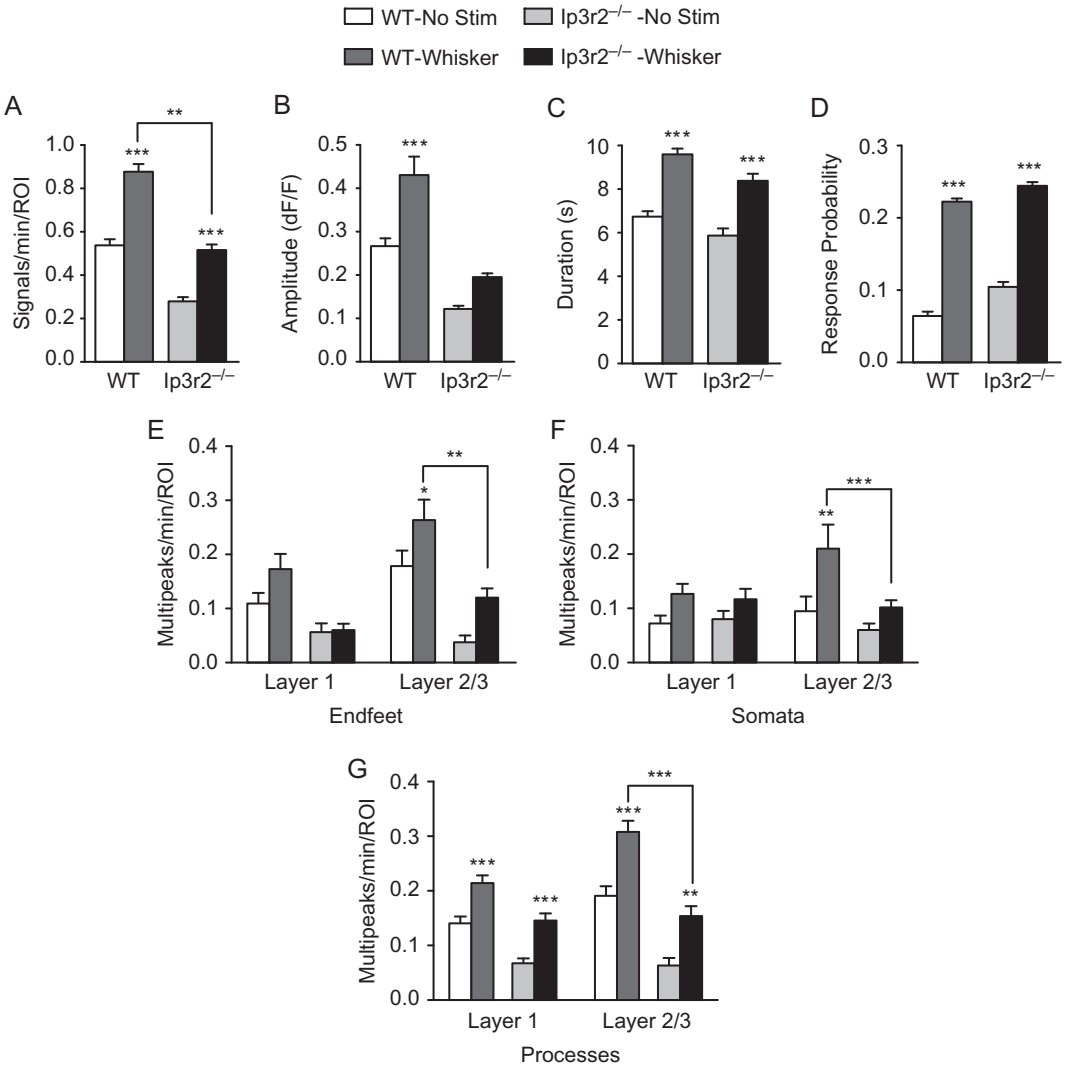

Figure 6. Astrocyte ROIs from *Ip3r2*$^{-/-}$ mice respond to sensory stimulation, but have fewer multipeak signals. (*A–D*) Mean number of signals per minute, amplitude, duration, and response probability for responding ROIs from WT (n = 452 ROIs including endfeet, somata, and processes; 2 mice) and knockouts (*Ip3r2*$^{-/-}$; n = 349 ROIs including endfeet, somata, and processes; 3 mice) with or without whisker stimulation (90 Hz; 8 s). (*E–G*) Mean number of multipeaks per minute, averaged across trials from endfeet, somata, and process ROIs in layer 1 or layer 2/3 from WT and knockout mice with or without whisker stimulation (8 s). Bar graphs are uncorrected mean ± SEM. $^{*}P < 0.05$, $^{**}P < 0.01$, $^{***}P < 0.001$. Statistics calculated using linear mixed models. See also Supplementary Fig. S5.

and Day 4) or inconsecutive days (e.g., Day 0 and Day 18). ROIs within the 4 days group responded to stimulation at every time point (Day 0, 4, 18, and 67; Fig. 8C). Endfeet and somata were more stable with many ROIs responding to whisker stimulation on 3 (endfeet: ~31%, somata: ~16%) or 4 (endfeet: ~5%, somata: ~2%) imaging days. Processes were less stable with ~46% of ROIs responding only on 1 day and no ROIs responding on all 4 days. Responding ROIs from each time point and ROI type had a similar mean number of signals per minute across days (Fig. 8D; $P < 0.0001$ for each no stim to whisker comparison over all ROI types). Furthermore, the number of peak types (single-peaks, multipeaks, and plateaus) per minute was also consistent across time points (Supplementary Fig. S7A–C).

Discussion

Heterogeneous astrocyte calcium signals have been identified in vivo (Bonder and McCarthy 2014; Srinivasan et al. 2015); however, the nature of these signals in response to local synaptic activity remains unclear. We sought to characterize astrocyte calcium signaling in different subcellular compartments in terms of long-term stability and temporal synchronicity using chronic in vivo 2-photon imaging of GCaMP6s during sensory stimulation and innovative analysis tools. These tools combined anatomical information (somata and endfeet) and activity-based region of interest selection (processes) to identify spontaneous and stimulus-evoked activity in different compartments, measured over several months. We found that a relatively large subset of astrocyte regions responded to brief, physiologically relevant sensory stimulation (Figs 3 and 4); however, these changes were driven by deviations in the relative frequency of different peak types (Fig. 5) rather than changes in the shape of individual peaks (Supplementary Fig. S4). Knockout of IP_3 receptor 2 (IP3R2), which is known to reduce calcium release from the ER, revealed a decreased number of process ROIs and multipeak signals evoked by stimulation, but did not affect the astrocytic response to stimulation as a whole (Fig. 6 and Supplementary Fig. S5). Signal synchronicity also

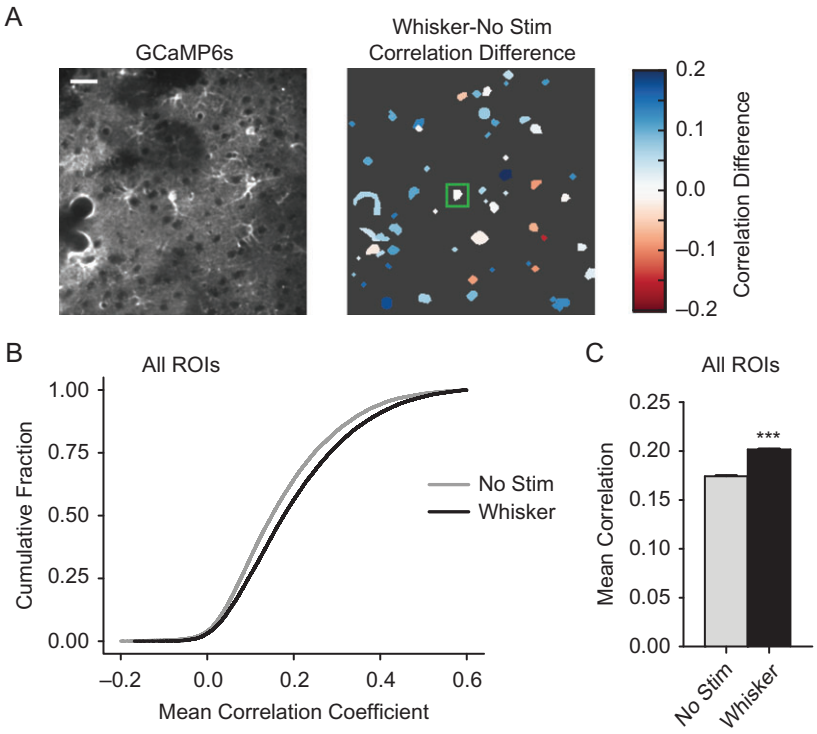

Figure 7. Astrocyte regions become more correlated upon sensory stimulation. (*A*) Mean pairwise Pearson correlation coefficients were calculated for all ROIs in a field of view with and without stimulation. Right: example ROI map of the mean correlation difference (whisker stimulation coefficients—no stimulation coefficients) based on the "seed" ROI (green square). Blue colors suggest greater correlation between ROIs during stimulation and red colors suggest greater correlation between ROIs during no stimulation trials. Scale bar is 30 μm. (*B*) Cumulative fraction of all pairwise ROI comparisons during no stimulation or 90 Hz whisker deflection trials (n = 27 307 pairs). (*C*) Mean correlation coefficient for all ROI pairs with and without whisker stimulation ($P < 0.0001$). Bar graph is uncorrected mean ± SEM. $^{*}P < 0.05$, $^{***}P < 0.001$. Statistics calculated using linear mixed models. See also Supplementary Fig. S5.

increased upon stimulation (Fig. 7 and Supplementary Fig. S6). When we monitored long-term stability of astrocyte responses in the same field of view, the overall response was constant across several months; however, different process regions were activated on different days (Fig. 8 and Supplementary Fig. S7). These results suggest that astrocytes may stably encode local neuronal activation through distinct calcium signal peak types and coordinated activity throughout the astrocytic network, but that the location of this activity within ramified astrocyte structures may change with time.

GECIs have revolutionized astrocyte calcium imaging by providing better labeling of fine process structures compared with calcium indicator dyes that primarily label the soma (Shigetomi et al. 2013); however, the characteristics of calcium signals that have been described vary depending on the GECI used. Early GECIs, such as Yellow Cameleon 3.60 and GCaMP3, have modest signal-to-noise ratios and relatively low affinity for calcium, which limited detection of spontaneous calcium microdomains within ramified astrocyte processes (Atkin et al. 2009; Paukert et al. 2014). High-affinity genetic calcium indicators, such as Yellow Cameleon Nano50, detect long (~70 s) spontaneous calcium signals within astrocyte processes (Kanemaru et al. 2014), which may reflect saturation of this sensor, making it difficult to elucidate individual peaks of different types. GCaMP6s is well suited for calcium imaging within astrocyte subcellular domains due to its strong signal-to-noise ratio and dissociation constant of 144 nM (Chen et al. 2013), which is within the astrocyte intracellular calcium concentration range (Zheng et al. 2015). With GCaMP6s, we observed localized, spontaneous calcium microdomains within process structures that have a higher mean amplitude (Fig. 1*E*) and a greater number of signals (Fig. 1*D*) than endfeet or somata, comparable to previous reports with other calcium indicators and in other brain regions (Shigetomi et al. 2013; Gee et al. 2014; Kanemaru et al. 2014; Otsu et al. 2015; Srinivasan et al. 2015; Tang et al. 2015). A previous study has also detected 3 different populations of GCaMP6s peaks in astrocytes: single-peaks, multipeaks, and plateaus (Bonder and McCarthy 2014). We found that multipeaks were the most common peak type in fine processes, while plateaus predominated in endfeet and somata (Fig. 1*K*). Singlepeaks were found in all cellular regions (endfeet, somata, and processes) and the dynamics of these peaks were similar to other reports (Bonder and McCarthy 2014).

Previously, Takata and Hirase (2008) used Oregon Green BAPTA 1-AM (OGB1) to visualize rat cortical astrocyte calcium signals in vivo and reported that somata in cortical layer 1 were more spontaneously active than somata in layer 2/3. We did not detect significant differences in somata, processes, or endfeet spontaneous activity between layer 1 and 2/3 (Supplementary Fig. S1A–C), though layer 1 somata tended to have more signals per minute (Supplementary Fig. S1A). Takata and Hirase (2008) also reported that more astrocytes are present in layer 1 than layer 2/3 of the rat cortex, but we did not observe a difference in the number of astrocytes/mm^2 in our mice (Supplementary Fig. S1*D*). These differences between rat and mouse cortical cyto-architectures could account for the discrepancies between our results.

Mice use their whiskers for vibrotactile perception mediated by high frequency changes in whisker position (Wolfe et al. 2008;

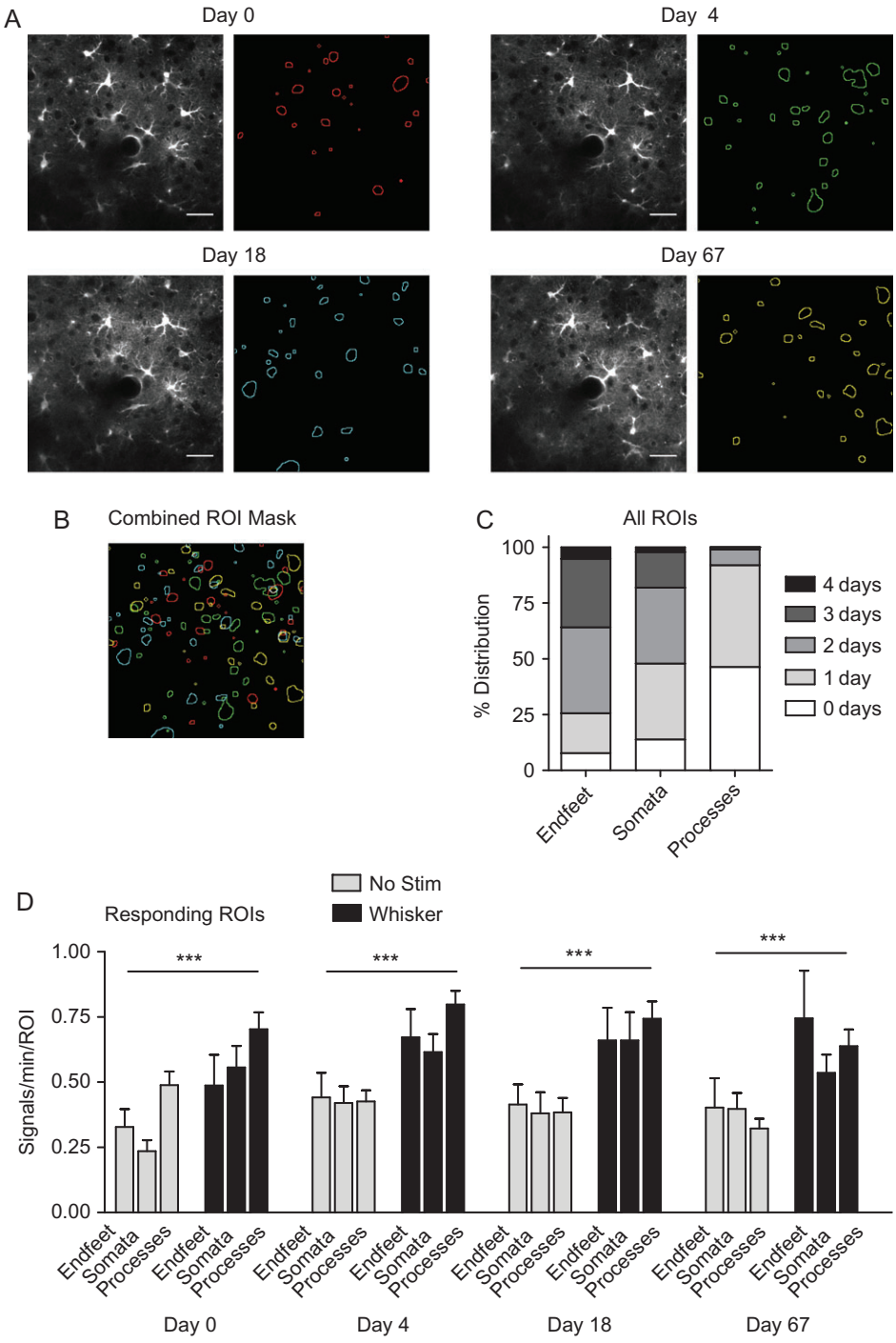

Figure 8. Astrocyte calcium responses are stable during chronic imaging. (*A*) Example images from the same astrocytes on different days (left) and contour outline of automated process ROI masks (right). Scale bar is 30 μm. (*B*) Combined ROI masks from (*A*) were used to identify overlapping regions. (*C*) The population distribution of the response frequency (number of days) for each ROI type (endfeet, somata, and processes). (*D*) Mean number of signals per minute for responding ROIs from each ROI type ($P < 0.0001$; endfeet, somata, and processes; 5 mice). Bar graphs are uncorrected mean ± SEM. ***$P < 0.001$. Statistics calculated using linear mixed models. See also Supplementary Fig. S6.

Jadhav et al. 2009; Mayrhofer et al. 2015). Recently, our group characterized the neuronal population response to increasing frequencies of whisker deflection and found that while many neurons respond weakly to stimulation, a subset of highly responding neurons (~3%) reliably discriminate different stimuli (Mayrhofer et al. 2015). In astrocytes, spontaneous signals tended to mask sensory stimulation-evoked activity within the population, particularly from whisker stimuli (Fig. 3C). We identified subcellular astrocyte regions that responded to sensory stimulation with a peak in the activity window, and these regions tended to be less spontaneously active and respond with more signals to different frequencies of stimulation (Fig. 3D). Based on the response probability (Fig. 3G), responding ROIs were more likely to have a peak in the activity window,

but they did not respond in every trial on average, possibly due to adaptation or a local "refractory" period within the astrocyte. This refractory period may reflect local receptor inactivation in highly responsive areas, and favor activation of other regions at later times. In a previous study using different frequencies of whisker stimulation for 1 min, local field potentials and astrocyte somata calcium responses peaked at 5 Hz and decreased at 10 Hz, which they attributed to neuronal adaptation (Wang et al. 2006). While we chose to use higher frequencies of stimulation that mimic "stick-slip" events from whisking on textured surfaces, we also limited stimulation to much shorter epochs (1 or 8 s) that reliably produce field potential spikes and calcium transients within neurons (Khatri et al. 2004; Musall et al. 2014; Mayrhofer et al. 2015). During this type of pulsatile whisker stimulation, neuronal adaptation occurs within the first few pulses and the number of spikes per pulse decreases, particularly at higher frequencies (Khatri et al. 2004; Fraser et al. 2006; Musall et al. 2014). However, neuronal responses remain locked to the pulsatile stimulus (Ewert et al. 2008) and are reproducible across many trials (Mayrhofer et al. 2015). While we did not observe a decrease in astrocyte responses with increasing whisker stimulation frequencies, neuronal adaptation could explain why the astrocytic response was not directly proportional to the stimulation intensity (10–90 Hz stimulation; Fig. 3*D*–*F*).

In terms of astrocyte compartments, a recent study compared calcium signals (from GCaMP5G) in astrocyte processes and somata during whisker stimulation and they found that somata and processes had similar mean amplitudes with a signal delay of ~25 s after the start of stimulation (Gee et al. 2014). We also found that somata, processes, and endfeet had a similar mean signal onset (~15 s), though peaks occurred earlier after the start of stimulation. Unlike Gee et al. (2014), we did not observe similar somata and process signal amplitudes (Fig. 4*D*). We attribute this to the prevalence of low-amplitude plateau signals in somata ROIs (Fig. 5*H*). We also observed similar response probabilities in endfeet, somata, and processes (Fig. 4*F*), suggesting that the stimulus response was analogous across ROI types. When considering ROI area, responding process ROIs had a larger mean area than spontaneous process ROIs (Fig. 4*B*), similar to recent observations of light-evoked astrocyte responses in the visual cortex (Asada et al. 2015). A larger area could reflect greater propagation of signals in response to stimulation. Processes have a close proximity to synapses, and the size of astrocyte domain activation could be an integral feature of how astrocytes encode local synaptic activity. It is also worth noting that anesthetics can inhibit astrocyte calcium signals (Thrane et al. 2012), which could have suppressed the calcium responses in our experiments. However, we found that the responses were consistent across animals under isoflurane anesthesia. Future studies in awake, behaving animals that simultaneously monitor local neuronal and astrocytic calcium signals will help to better elucidate the time course and possible coordinated activity between these 2 cell populations.

When considering individual calcium signals, the shape of peaks (duration and amplitude) did not change upon sensory stimulation. However, we observed an increased number of multipeak and plateau signals, which directly accounts for the differences in mean amplitude and duration that we detected between somata and processes. Somata (particularly in layer 2/3) had more plateau signals, which were of longer duration and lower amplitude, while multipeaks occurred more frequently in processes (Fig. 5), which increased the mean amplitude and number of signals per minute. Different peak types could explain how astrocytes integrate synaptic activity and may represent diverse mechanisms of signaling. Numerous pathways are known to increase intracellular calcium in astrocytes including various ion channels and calcium release from ER stores through G-protein-coupled receptor (GPCR)-mediated IP_3 signaling or calcium-induced calcium release via ryanodine receptors (Parpura et al. 2011). We specifically examined IP_3 signaling and found that, similar to a previous study (Srinivasan et al. 2015), *Ip3r2*$^{-/-}$ mice had fewer spontaneous singlepeaks and multipeaks. These mice also had less sensory-stimulus-evoked multipeak signals (Fig. 6 and Supplementary Fig. S5). This suggests that GPCR activation and IP_3-mediated release of ER calcium stores contribute to these types of signals. However, it is important to note that even though there were fewer process ROIs detected and less multipeak signals, the sensory-evoked astrocytic responses were not abolished in these animals and we could identify responding regions in all subcellular compartments without a change in response probability between knockouts and littermate controls (Fig. 6*D*). This indicates that other cellular mechanisms have a role in astrocyte sensory-evoked calcium signaling. Further pharmacological or transgenic mouse studies targeting different pathways of activation will help to elucidate the contribution of these pathways to astrocyte calcium peak types.

We also observed a weak signal correlation between spontaneous astrocyte signals within the same field of view, which was similar to a previous report of correlated OGB1 activity in somata (Takata and Hirase 2008). The pairwise correlations, particularly for responding ROIs, increased upon stimulation, which suggests the population becomes more synchronous (Fig. 7). Astrocyte populations throughout the cortex are known to display widespread, coordinated calcium signaling and synchronicity, particularly within somata, in response to norepinephrine from the locus coeruleus (Ding et al. 2013; Paukert et al. 2014) and acetylcholine from the nucleus basalis (Takata et al. 2011). In the present study, we did not observe sensory-stimulus-evoked calcium signals outside the corresponding somatosensory region (Supplementary Fig. S3), suggesting these neuromodulatory pathways are not recruited by our stimulation paradigms. Increased astrocyte synchronicity after sensory stimulation could be an important component of astrocyte information processing and reflect barrel cortex circuit connectivity.

To our knowledge, we also present here the first chronic study in vivo of astrocyte calcium signals in the same population over time (Fig. 8). Endfeet and somata responded more stably to whisker stimulation across multiple days (Fig. 8*C*). Process signals tended to occur in a particular region only in a single session. It is possible that different processes are activated at different times based on the local synaptic responses (Grienberger and Konnerth 2012). Our group has previously shown that a sparse population of neurons responds reliably over different time points to whisker stimulation (Margolis et al. 2012; Mayrhofer et al. 2015). However, different synapses within the arbor of these neurons could be activated at each time point and this may cause the spatial diversity we observed in responding astrocyte processes. Signals within astrocyte processes may also induce responses in the soma and/or endfeet through second messenger cascades, allowing astrocytes to translate signals from different processes into similar calcium responses in somata or endfeet. This would account for the stable responses we observed in somata and endfeet on multiple days and could be an important feature of how astrocytes integrate synaptic information throughout the cell.

Our results provide new insights into the nature of astrocyte calcium signaling in response to sensory stimulation, particularly in terms of subcellular astrocyte compartmentation and different peak types. A clearer picture of calcium signaling within somatosensory astrocytes is starting to emerge: somata and endfeet respond stably to sensory stimulation over time with more plateau signals and increased synchronicity. Processes have the greatest response to sensory stimulation and favor oscillating multipeaks, but these signals are less synchronous and do not occur in the same process in different sessions. This helps to clarify astrocyte calcium signal heterogeneity, but raises fundamental questions about how astrocytes encode local neuronal network activity through different calcium signal peaks within different cellular compartments. Further studies correlating astrocyte and neuronal activity are now needed to better understand how astrocytes integrate synaptic frequencies.

Supplementary Material

Supplementary data is available at *Cerebral Cortex* online.

Funding

Heart and Stroke Foundation of Canada (Junior Personnel Award to J.L.S.); the University of Zurich (Forschungskredite to J.L.S., A.S.S., and M.J.P.B.) and EMBO (Long-Term Fellowship to A.S.S.).

Notes

We would like to thank Ladina Hösli, Jean-Marc Fritschy, and his laboratory for help with immunohistochemistry and Steven Brown and his group for molecular biology support. We would also like to thank Andrea Volterra and Ju Chen for the *Ip3r2* mouse line. B.W. is a member of the Clinical Research Priority Program of the University of Zurich on Molecular Imaging. The authors declare no competing financial interests. *Conflict of Interest*: None declared.

References

Appaix F, Girod S, Boisseau S, Römer J, Vial JC, Albrieux M, Maurin M, Depaulis A, Guillemain I, van der Sanden B. 2012. Specific in vivo staining of astrocytes in the whole brain after intravenous injection of sulforhodamine dyes. PLoS One. 7:1–13.

Asada A, Ujita S, Nakayama R, Oba S, Ishii S, Matsuki N, Ikegaya Y. 2015. Subtle modulation of ongoing calcium dynamics in astrocytic microdomains by sensory inputs. Physiol Rep. 3:e12454.

Atkin SD, Patel S, Kocharyan A, Holtzclaw LA., Weerth SH, Schram V, Pickel J, Russell JT. 2009. Transgenic mice expressing a cameleon fluorescent Ca2+ indicator in astrocytes and Schwann cells allow study of glial cell Ca2+ signals in situ and in vivo. J Neurosci Methods. 181:212–226.

Bates D, Mächler M, Bolker B, Walker S. 2015. Fitting linear mixed-effects models using lme4. J Stat Softw. 67:1–48.

Bonder DE, McCarthy KD. 2014. Astrocytic Gq-GPCR-linked IP3R-dependent Ca2+ signaling does not mediate neurovascular coupling in mouse visual cortex in vivo. J Neurosci. 34: 13139–13150.

Chen T-W, Wardill TJ, Sun Y, Pulver SR, Renninger SL, Baohan A, Schreiter ER, Kerr RA, Orger MB, Jayaraman V, et al. 2013. Ultrasensitive fluorescent proteins for imaging neuronal activity. Nature. 499:295–300.

Di Castro MA, Chuquet J, Liaudet N, Bhaukaurally K, Santello M, Bouvier D, Tiret P, Volterra A. 2011. Local Ca2+ detection and modulation of synaptic release by astrocytes. Nat Neurosci. 14:1276–1284.

Ding F, O'Donnell J, Thrane AS, Zeppenfeld D, Kang H, Xie L, Wang F, Nedergaard M. 2013. α1-Adrenergic receptors mediate coordinated Ca2+ signaling of cortical astrocytes in awake, behaving mice. Cell Calcium. 54:387–394.

Ellefsen KL, Settle B, Parker I, Smith IF. 2014. An algorithm for automated detection, localization and measurement of local calcium signals from camera-based imaging. Cell Calcium. 56:147–156.

Ewert TAS, Vahle-Hinz C, Engel AK. 2008. High-frequency whisker vibration is encoded by phase-locked responses of neurons in the rat's barrel cortex. J Neurosci. 28:5359–5368.

Fraser G, Hartings JA, Simons DJ. 2006. Adaptation of trigeminal ganglion cells to periodic whisker deflections. Somatosens Mot Res. 23:111–118.

Gee JM, Smith NA, Fernandez FR, Economo MN, Brunert D, Rothermel M, Morris SC, Talbot A, Palumbos S, Ichida JM, et al. 2014. Imaging activity in neurons and glia with a Polr2a-based and Cre-dependent GCaMP5G-IRES-tdTomato reporter mouse. Neuron. 83:1058–1072.

Grienberger C, Konnerth A. 2012. Imaging calcium in neurons. Neuron. 73:862–885.

Hothorn T, Bretz F, Westfall P. 2008. Simultaneous inference in general parametric models. Biometrical J. 50:346–363.

Jadhav SP, Wolfe J, Feldman DE. 2009. Sparse temporal coding of elementary tactile features during active whisker sensation. Nat Neurosci. 12:792–800.

Kanemaru K, Sekiya H, Xu M, Satoh K, Kitajima N, Yoshida K, Okubo Y, Sasaki T, Moritoh S, Hasuwa H, et al. 2014. In vivo visualization of subtle, transient, and local activity of astrocytes using an ultrasensitive Ca2+ indicator. Cell Rep. 8: 311–318.

Khatri V, Hartings JA, Simons DJ. 2004. Adaptation in thalamic barreloid and cortical barrel neurons to periodic whisker deflections varying in frequency and velocity. J Neurophysiol. 92:3244–3254.

Lee Y, Messing A, Su M, Brenner M. 2008. GFAP promoter elements required for region-specific and astrocyte-specific expression. Glia. 56:481–493.

Li X, Zima AV, Sheikh F, Blatter LA, Chen J. 2005. Endothelin-1-induced arrhythmogenic Ca2+ signaling is abolished in atrial myocytes of inositol-1,4,5-trisphosphate(IP3)-receptor type 2-deficient mice. Circ Res. 96:1274–1281.

Mächler P, Wyss MT, Elsayed M, Stobart J, Gutierrez R, Von Faber-Castell A, Kaelin V, Zuend M, San Martín A, Romero-Gómez I, et al. 2016. In vivo evidence for a lactate gradient from astrocytes to neurons. Cell Metab. 23:94–102.

Margolis DJ, Lütcke H, Schulz K, Haiss F, Weber B, Kügler S, Hasan MT, Helmchen F. 2012. Reorganization of cortical population activity imaged throughout long-term sensory deprivation. Nat Neurosci. 15:1539–1546.

Mayrhofer JM, Haiss F, Helmchen F, Weber B. 2015. Sparse, reliable, and long-term stable representation of periodic whisker deflections in the mouse barrel cortex. Neuroimage. 115:52–63.

Musall S, Von Der Behrens W, Mayrhofer JM, Weber B, Helmchen F, Haiss F. 2014. Tactile frequency discrimination is enhanced by circumventing neocortical adaptation. Nat Neurosci. 17:1567–1573.

Navarrete M, Perea G, de Sevilla DF, Gómez-Gonzalo M, Núñez A, Martín ED, Araque A. 2012. Astrocytes mediate in vivo cholinergic-induced synaptic plasticity. PLoS Biol. 10:e1001259.

Nizar K, Uhlirova H, Tian P, Saisan P A., Cheng Q, Reznichenko L, Weldy KL, Steed TC, Sridhar VB, MacDonald CL, et al. 2013. In vivo stimulus-induced vasodilation occurs without IP3 receptor activation and may precede astrocytic calcium increase. J Neurosci. 33:8411–8422.

Otsu Y, Couchman K, Lyons DG, Collot M, Agarwal A, Mallet J-M, Pfrieger FW, Bergles DE, Charpak S. 2015. Calcium dynamics in astrocyte processes during neurovascular coupling. Nat Neurosci. 18:210–218.

Parpura V, Grubisic V, Verkhratsky A. 2011. Ca2+ sources for the exocytotic release of glutamate from astrocytes. Biochim Biophys Acta. 1813:984–991.

Paukert M, Agarwal A, Cha J, Doze VA, Kang JU, Bergles DE. 2014. Norepinephrine controls astroglial responsiveness to local circuit activity. Neuron. 82:1263–1270.

Petersen CCH. 2007. The functional organization of the barrel cortex. Neuron. 56:339–355.

Petravicz J, Fiacco T a, McCarthy KD. 2008. Loss of IP3 receptor-dependent Ca2+ increases in hippocampal astrocytes does not affect baseline CA1 pyramidal neuron synaptic activity. J Neurosci. 28:4967–4973.

Schneider CA, Rasband WS, Eliceiri KW. 2012. NIH image to ImageJ: 25 years of image analysis. Nat Methods. 9: 671–675.

Shigetomi E, Bushong EA, Haustein MD, Tong X, Jackson-Weaver O, Kracun S, Xu J, Sofroniew M V, Ellisman MH, Khakh BS. 2013. Imaging calcium microdomains within entire astrocyte territories and endfeet with GCaMPs expressed using adeno-associated viruses. J Gen Physiol. 141:633–647.

Srinivasan R, Huang BS, Venugopal S, Johnston AD, Chai H, Zeng H, Golshani P, Khakh BS. 2015. Ca2+ signaling in astrocytes from Ip3r2$^{-/-}$ mice in brain slices and during startle responses in vivo. Nat Neurosci. 18:708–717.

Takata N, Hirase H. 2008. Cortical layer 1 and layer 2/3 astrocytes exhibit distinct calcium dynamics in vivo. PLoS One. 3: e2525.

Takata N, Mishima T, Hisatsune C, Nagai T, Ebisui E, Mikoshiba K, Hirase H. 2011. Astrocyte calcium signaling transforms cholinergic modulation to cortical plasticity in vivo. J Neurosci. 31:18155–18165.

Takata N, Nagai T, Ozawa K, Oe Y, Mikoshiba K, Hirase H. 2013. Cerebral blood flow modulation by basal forebrain or whisker stimulation can occur independently of large cytosolic Ca2+ signaling in astrocytes. PLoS One. 8:4–9.

Tang W, Szokol K, Jensen V, Enger R, Trivedi CA, Hvalby O, Helm PJ, Looger LL, Sprengel R, Nagelhus EA. 2015. Stimulation-evoked Ca2+ signals in astrocytic processes at hippocampal CA3-CA1 synapses of adult mice are modulated by glutamate and ATP. J Neurosci. 35:3016–3021.

Thrane AS, Rangroo Thrane V, Zeppenfeld D, Lou N, Xu Q, Nagelhus EA, Nedergaard M. 2012. General anesthesia selectively disrupts astrocyte calcium signaling in the awake mouse cortex. Proc Natl Acad Sci. 109:18974–18979.

Volterra A, Liaudet N, Savtchouk I. 2014. Astrocyte Ca(2+) signalling: an unexpected complexity. Nat Rev Neurosci. 15: 327–335.

Wang X, Lou N, Xu Q, Tian G-F, Peng WG, Han X, Kang J, Takano T, Nedergaard M. 2006. Astrocytic Ca2+ signaling evoked by sensory stimulation in vivo. Nat Neurosci. 9: 816–823.

Wolfe J, Hill DN, Pahlavan S, Drew PJ, Kleinfeld D, Feldman DE. 2008. Texture coding in the rat whisker system: slip-stick versus differential resonance. PLoS Biol. 6:1661–1677.

Zheng K, Bard L, Reynolds JP, King C, Jensen TP, Gourine AV, Rusakov DA. 2015. Time-resolved imaging reveals heterogeneous landscapes of nanomolar Ca2+ in neurons and astroglia. Neuron. 88:277–288.